EAI Endorsed Transactions
on Sustainable Manufacturing and Renewable Energy Research Article EAI.EU

Influence of Magnetic Fields on the Microstructure and Mechanical Properties of MIG Welds

Tan Nam Le[1,2], Thanh Long Bui[1,2], Quang Thanh Le[3], Phat Dat Huynh[1,2] and Thanh Phong Nguyen[1,2*]

[1] Faculty of Mechanical Engineering, Ho Chi Minh City University of Technology (HCMUT), 268 Ly Thuong Kiet Street, District 10, Ho Chi Minh City, Vietnam

[2] Viet Nam National University Ho Chi Minh City, Linh Trung Ward, Thu Duc District, Ho Chi Minh City, Vietnam
[3] Faculty of Mechanical Engineering, Ho Chi Minh City University of Transport, Ho Chi Minh, Viet Nam

Abstract

This study investigates the impact of magnetic fields on the microstructure and mechanical properties of Metal Inert Gas (MIG) welds. Steel plate samples were welded under the influence of a magnetic field generated by permanent magnets, with simulations and experimental analyses used to evaluate weld quality. Key parameters such as magnetic field strength, magnet rotation speed, and distance were varied to assess their effects on the weld structure. The results revealed that applying a dynamic magnetic field improves weld penetration, alters grain structure, and reduces defects, enhancing mechanical strength and weld integrity. Finite element modeling was employed to simulate the effects of rotating magnets on the welding area, showing a uniform temperature distribution and significant changes in the fluid flow of the molten pool. These findings provide insights into optimizing welding parameters and demonstrate the potential for using magnetic fields to enhance welding processes, offering practical applications for advanced manufacturing.

Keywords: Magnetic Field Effects, MIG Welding, Weld Microstructure, Mechanical Properties, Finite Element Modeling.

Received on 14 11 2024, accepted on 16 11 2024, published on 20 11 2024

doi: 10.4108/eetsmre.7836

1. Introduction

Welding is an essential technique for joining metals in various manufacturing sectors due to its cost-effectiveness and efficiency compared to other methods like casting and riveting. Critical factors such as weld width, depth, and the microstructural characteristics of the metal at the joint influence the mechanical properties of the weld. Parameters such as welding current, speed, voltage, and external magnetic fields can significantly impact weld quality and are adjustable to enhance mechanical strength. Among welding methods, Metal Inert Gas (MIG) welding is widely used for its speed, cost-effectiveness, and simplicity. It involves using a consumable metal wire electrode and a protective inert gas shield, forming reliable welds with minimal post-treatment [1, 2]. However, high heat input and rapid cooling can lead to residual stresses and deformation, necessitating efforts to predict and mitigate welding defects [3, 4].

Numerical methods have been developed to analyze factors like melt pool geometry, residual stresses, and weld deformations. For instance, Walker et al. [5] modeled heat sources to predict melt pool geometry, while Hu et al. [6] investigated droplet dynamics, temperature distribution, and fluid flow within the weld pool. The use of external magnetic fields has emerged as a promising approach to enhance weld characteristics. Studies by Wang et al. [7] demonstrated that axial magnetic fields increase weld bead morphology by raising the temperature near the tungsten tip, providing more energy to the anode. Lin et al. [8] showed that external electromagnetic fields (EMFs) improve temperature distribution uniformity and fluid flow, although the overall impact on the molten weld pool remained limited. Further,

*Corresponding author. Email: ntphong.sdh241@hcmut.edu.vn

Nomura et al. [9, 10] used permanent magnets arranged circularly to significantly enhance weld penetration depth.

MIG welding is versatile, suitable for a wide range of materials and thicknesses. However, challenges such as weld cracking, metal porosity, and hardening can arise, particularly with high-carbon steels [11]. Methods to improve the process, including the application of magnetic fields to influence features such as wire melting rate, bead shape, and temperature distribution, have shown positive results [12-14]. Applying magnetic fields can generate Lorentz forces that stir the molten pool, enhancing the weld's microstructure and mechanical properties [15, 16]. This study investigates the effects of a rotating magnet model, creating a dynamic magnetic field around the welding zone, to optimize weld quality through improved droplet formation and weld pool structure.

This study examines the influence of a dynamic magnetic field, created by rotating permanent magnets, on the microstructure and mechanical properties of MIG welds. By analyzing the effects of magnetic field strength, magnet distance, and rotation speed, the goal is to optimize weld quality and provide a basis for enhancing welding technologies in manufacturing.

2. Numerical model

The study analyzes the effects of a magnetic field on weld properties using a computational domain with dimensions of 300×300 mm, encompassing the magnet system, welding head, and workpiece. A height of 250 mm is utilized to ensure complete coverage of all simulated elements.

2.1. Analysis process

To evaluate the influence of a dynamic magnetic field on weld quality and shape, the experimental model uses NdFeB35 permanent magnets, each measuring 40x25x10 mm, arranged in two layers beneath the workpiece. The magnetic poles are configured as depicted in Figure 1. The welding sample, conforming to ASTM standards, has a thickness of 5 mm, with a 2 mm gap between the magnets and the bottom of the steel plate. During the welding process, the welding head remains fixed at a predetermined position, while the magnets rotate at a constant speed beneath the workpiece. Prior to welding, all sample surfaces are polished with 400-grit sandpaper and thoroughly cleaned.

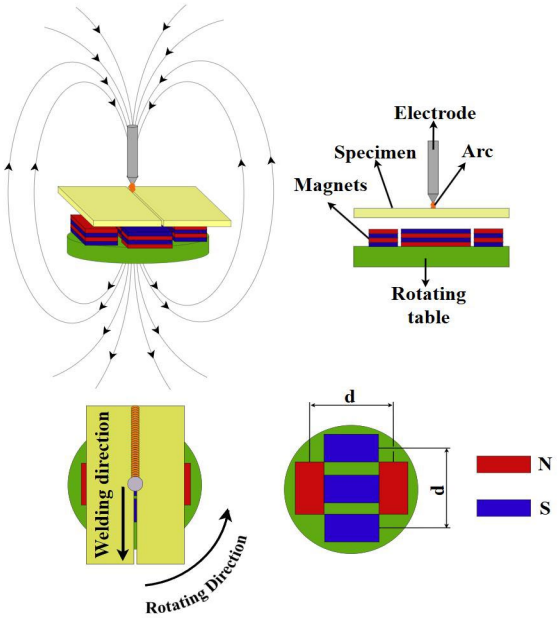

Figure 1. Experimental setup diagram

The accuracy of the simulated model is highly dependent on the finite element analysis method employed. Element adjustments during the simulation allow for results that closely match actual values. The fineness of the mesh is varied based on computational requirements. For this study, a 3D model is utilized, necessitating a division into free tetrahedral elements to balance accuracy and computational resources. To optimize results, the magnets and the weld position are meshed with higher precision. The final mesh configuration consists of 129,840 tetrahedral elements, 10,402 faces (surface elements of the 3D model), and 1,048 edges (elements along the model's boundaries), as illustrated in Figure 2.

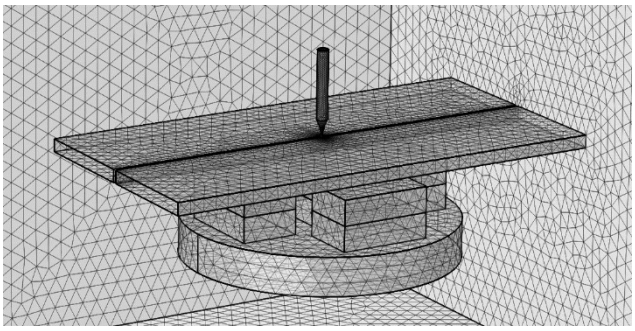

Figure 2. Mesh results

2.2. Material

The stainless steel AISI 304 used in the experiment has a thickness of 5 mm, with its chemical composition detailed in Table 1.

Table 1. Chemical composition of AISI 304 Stainless Steel (%)

C	Cr	Ni	Mo	Mn	Si	Cu
0.08	19.5-22.0	9.0-11.0	0.75	1.0-2.5	0.30-0.65	0.75

The shielding gas used can be either argon or helium. Helium offers superior thermal conductivity and generates a higher-temperature arc compared to argon, leading to improved penetration. Consequently, helium was chosen as the shielding gas for this experiment.

2.3. Solution procedure

Weld defects, such as humping and undercutting, can arise during the arc welding process [17]. These defects are influenced by various factors, including welding speed, power, shielding gas, and the properties of the base metal [18]. Demeyesus et al. [19] conducted experiments on welding stainless steel 304 to determine optimal welding parameters for enhancing ultimate tensile strength, bend strength, and Rockwell hardness of TIG welds. The experiments utilized a current of 110 A, a welding speed of 13.86 cm/min, a voltage of 17.5 V, and a shielding gas flow rate of 7.5 L/min. In this study, key parameters to be evaluated include the distance between magnets, rotation speed, and measurement of magnetic field intensity at the welding position. Each parameter is tested at three distinct levels, as detailed in Table 2.

Table 2. Levels of experimental parameters

Distance (mm)	65	71	77
Rotation Speed (RPM)	15	25	35
Measurement Position	1	2	3

During the simulation, magnetic field intensity is measured at three positions along the vertical axis, and the average value is used to determine optimal parameters. Following this, experiments are conducted to validate the simulation results. The measurement positions are illustrated in Figure 3.

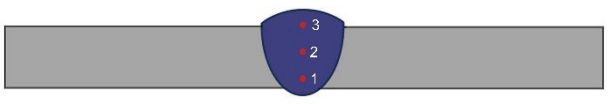

Figure 3. Measurement positions for magnetic field intensity

Beyond the influence of the magnetic field, welding speed is a critical factor that impacts the structural quality of the weld [20]. Consequently, it is essential to evaluate weld quality after the experimental process using different welding speeds.

Table 3. Experimental design matrix

N	Distance d (mm)	Rotation Speed (RPM)	Position
1	77	25	3
2	77	15	2
3	71	15	3
4	71	15	1
5	71	25	2
6	71	35	3
7	77	15	2
8	71	35	1
9	65	25	1
10	71	25	2
11	65	35	2
12	65	15	2
13	71	25	2
14	65	25	3
15	77	25	1

Using the experimental design matrix in Table 3, simulations were conducted across various scenarios. Subsequently, welding was performed on 15 steel plate samples, followed by detailed analysis and evaluation. The results were compared with simulation data to assess the accuracy and effectiveness of the method.

3. Result and discussion

Using the 3D model and the specified parameters for magnet characteristics and the welding sample, the magnetic field distribution within the welding region is depicted in Figure 4 and Figure 5. The maximum magnetic flux density, approximately 1.93T, is observed on the upper surface of the magnet and decreases as it approaches the weld position.

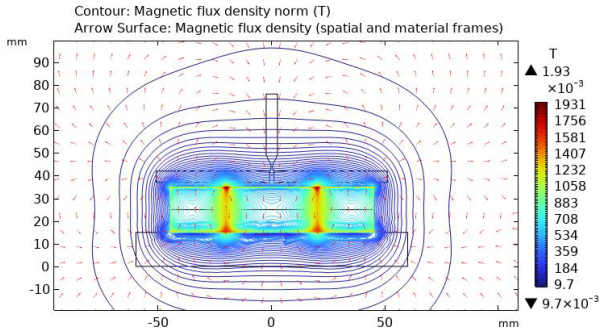

Figure 4. Magnetic field density at the welding position in the OXY Section

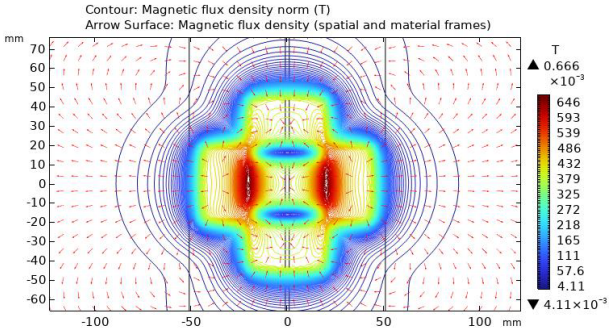

Figure 5. Magnetic Field Density at the Welding Position in the OXZ Section

The results indicate that magnetic flux lines become denser as the distance to the magnet's surface decreases. Arrows illustrate the direction of the magnetic flux. During welding, stronger magnetic forces exert a greater influence on particle speed and trajectory. This rapid crystallization process significantly affects the weld's microstructure. At the welding position, the magnetic field intensity ranges from approximately 0.290 to 0.326T. Detailed measurements are provided in Table 4.

Table 4. Magnetic field values

N	Distance d (mm)	Rotation Speed (RPM)	Position	ΔT (T)
1	77	25	3	0.2865
2	77	15	2	0.3049
3	71	15	3	0.312
4	71	15	1	0.3552
5	71	25	2	0.3223
6	71	35	3	0.312
7	77	15	2	0.3233
8	71	35	1	0.3557
9	65	25	1	0.3904
10	71	25	2	0.3423
11	65	35	2	0.3492
12	65	15	2	0.3493
13	71	25	2	0.3261
14	65	25	3	0.3249
15	77	25	1	0.3126

Table 5 presents data analyzed from the regression equation developed during the study. It includes input factors such as distance, rotation speed, and measurement position, along with the corresponding magnetic field values. The coefficients indicate the impact of these factors on the response variable y.

The constant coefficient (Coef) is 0.33111, with a very high T-Value (158.81) and a P-Value of 0 (very small). This indicates that the constant is highly statistically significant, providing a strong baseline value in the model for prediction.

The Coef of x_1 is -0.02331, with an SE Coef (standard error of the coefficient) of 0.00285. The T-Value is -8.17, and the P-Value is 0, indicating that x_1 is highly statitically significant.

The negative coefficient indicates that x_1 has an inverse effect on the outcome. As x_1 increases, the dependent variable decreases by -0.02331 units per one-unit increase in x_1.

The Variance Inflation Factor (VIF) is 1, showing no multicollinearity between x_1 and other variables.

Table 5. Coded coefficients

Term	Coef	SE-Coef	T-Value	P-Value	VIF
Constant	0.331	0.002	158.81	0	
x_1	-0.023	0.003	-8.17	0	1
x_3	-0.022	0.003	-7.82	0	1
$x_1 * x_3$	0.009	0.004	2.44	0.033	1

The analysis results are summarized in the ANOVA table, detailing factors such as Degrees of Freedom (DF), Adjusted Sum of Squares (Adj SS), and F-Values. DF represents the number of values that can vary independently without altering the total number of observations, helping to determine the model's complexity and each factor's contribution. Adj SS reflects the total variation in the response variable explained by each factor or interaction, accounting for the influence of other factors. The F-Value, which is the ratio of a factor's variation to random error variation, tests the factor's significance; a high F-Value suggests a strong impact, indicating that the factor should remain in the model. Table 6 serves as a basis for evaluating the relationships between the independent variables and the response.

Table 6. Analysis of variance

Source	DF	Adj SS	Adj MS	F-Value	P-Value
Model		0.0087	0.0029	44.57	0
Linear	2	0.0083	0.0042	63.88	0
x_1	1	0.0043	0.0043	66.68	0
x_3	1	0.0039	0.004	61.08	0
2-Way Interaction	1	0.0003	0.0004	5.95	0.033
$x_1 * x_3$	1	0.0003	0.0004	5.95	0.033
Error	11	0.0007	0.0001		
Lack-of-Fit	8	0.0003	0.00004	0.31	0.92
Pure Error	3	0.0003	0.0001		
Total	14	0.0094			

The results indicate that the factors x_1, x_3 and the interaction $x_1 * x_3$ are all statistically significant, contributing to explaining the variability in the data. The high P-Value for Lack-of-Fit suggests that there is no significant difference between the model and the actual data, indicating that the model fits well without any indication of lack of fit. Based on the F-Values and P-Values, it can be concluded that this model has strong predictive power and effectively explains the variation in the dependent variable.

Table 5 and Table 6 show the regression equation was developed to represent the mathematical relationship between the magnetic field value at the welding position and the three factors: magnet system distance, rotation speed, and measurement position.

The equation is expressed as follows:

$$y = 0.885 - 0.00717x_1 - 0.1389\,x_3 + 0.001642\,x_1x_3$$

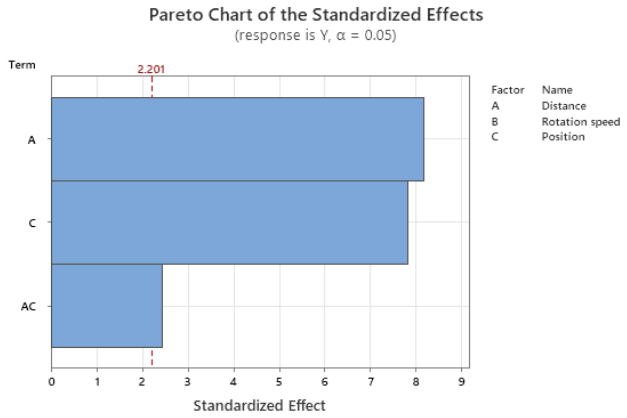

Figure 6. Pareto chart

At positions A and C in Figure 6, the standardized effects are the largest, surpassing the threshold of 2.201. This indicates that the measurement position is the most influential and statistically significant factor affecting the response variable. Additionally, the interaction between distance and measurement position (denoted as AC) also exceeds the threshold, signifying a significant interaction between these factors.

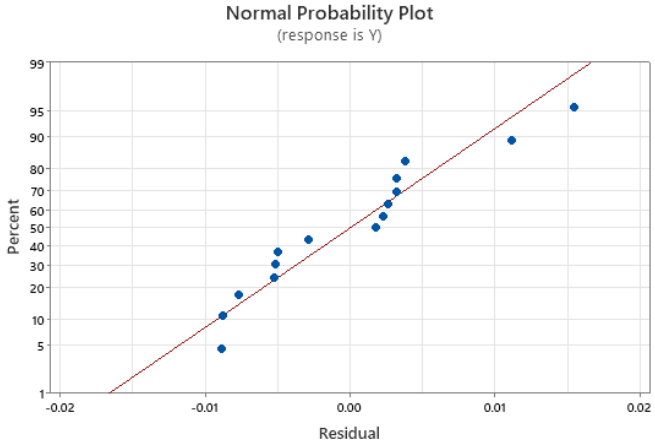

Figure 7. Normal probability plot

The data points in Figure 7 will be close to a red straight line, indicating that the data follows a normal distribution

Table 7. Statictical model and performance measurement

S	R-sq	R-sq(adj)	R-sq(pred)
0.0080751	92.40%	90.33%	82.92%

Table 7 show that the value of the standard deviation of residuals (S) at 0.0080751 indicates that the residuals' standard deviation is relatively low, suggesting a small error in the model. This implies that the model's predicted values are closely aligned with actual values, indicating a relatively high degree of accuracy. A small S value can suggest that the analytical model is suitable for predicting outcomes in the experimental process.

The R-squared (R^2) value of 92.40% implies that the model explains 92.4% of the variance in the data. A high R^2 (above 90%) suggests a strong model fit and high predictive capability.

The adjusted R-squared (R^2 adj) is 90.33%, slightly lower than R^2. This adjusted index accounts for the number of predictors in the model to prevent overfitting. With a value exceeding 90%, R^2(adj) indicates that the model retains a strong explanatory capacity without signs of overfitting, supporting the robust correlation between independent and dependent variables.

The predicted R-squared (R^2 pred) is 82.92%, which reflects the model's predictive ability for unobserved data. Although lower than R^2 and R^2(adj), this value remains high (over 80%), demonstrating the model's capacity to perform well on new data. This result is important for concluding that the model generalizes well and can be applied to predict values in other scenarios.

These results suggest that the model exhibits strong predictive value, with indices reaching reliable thresholds for supporting analysis and prediction, thereby enhancing the experimental process.

4. Conclusion

The analysis demonstrates that the model effectively explains variations in the response variable, with measurement position and its interaction with distance identified as critical factors influencing the outcome. Positions A and C exhibit the most substantial effects, emphasizing their significant impact. Additionally, the interaction between distance and measurement position suggests a complex relationship that warrants further study. The model's strong predictive capability is supported by exceptionally low P-Values for main effects and interactions, high R-squared values (92.4%), and low error variance, indicating a robust fit to the data. These results highlight the model's potential for accurate predictions and practical applications, providing valuable insights for enhancing measurement precision and analysis in similar contexts.

Acknowledgements.

We acknowledge the support of time and facilities from Ho Chi Minh City University of Technology (HCMUT), VNU-HCM for this study.

References

[1] Lostado Lorza, R., et al., Using Genetic Algorithms with Multi-Objective Optimization to Adjust Finite Element Models of Welded Joints. Metals, 2018. **8**(4): p. 230.

[2] Perić, M., et al., Numerical analysis of longitudinal residual stresses and deflections in a T-joint welded structure using a local preheating technique. Energies, 2018. **11**(12): p. 3487.

[3] Lostado Lorza, R., et al., Residual stresses with time-independent cyclic plasticity in finite element analysis of welded joints. Metals, 2017. **7**(4): p. 136.

[4] Xiong, Y., et al., The evolution of residual stress in rib-diaphragm joints of orthotropic steel decks subjected to thermal cutting and welding. Materials, 2020. **13**(17): p. 3804.

[5] Walker, T. and C. Bennett, An automated inverse method to calibrate thermal finite element models for numerical welding applications. Journal of Manufacturing Processes, 2019. **47**: p. 263-283.

[6] Hu, J. and H.-L. Tsai, Heat and mass transfer in gas metal arc welding. Part II: The metal. International Journal of Heat and Mass Transfer, 2007. **50**(5-6): p. 808-820.

[7] Chen, T., et al., Numerical study of DC argon arc with axial magnetic fields. Plasma Chemistry and Plasma Processing, 2015. **35**: p. 61-74.

[8] Wang, L., et al., Numerical simulation of coupled arc-droplet-weld pool behaviors during compound magnetic field assisted gas metal arc welding. AIP Advances, 2021. **11**(6).

[9] Nomura, K., K. Morisaki, and Y. Hirata, Magnetic control of arc plasma and its modelling. Welding in the World, 2009. **53**: p. R181-R187.

[10] Nomura, K., Y. Ogino, and Y. Hirata, Shape control of TIG arc plasma by cusp-type magnetic field with permanent magnet. Welding International, 2012. **26**(10): p. 759-764.

[11] Bachmann, M., et al., About the influence of a steady magnetic field on weld pool dynamics in partial penetration high power laser beam welding of thick aluminium parts. International Journal of Heat and Mass Transfer, 2013. **60**: p. 309-321.

[12] Mills, K. and B. Keene, Factors affecting variable weld penetration. International Materials Reviews, 1990. **35**(1): p. 185-216.

[13] Langenecker, B., Effects of ultrasound on deformation characteristics of metals. IEEE transactions on sonics and ultrasonics, 1966. **13**(1): p. 1-8.

[14] Fu, J., et al., Influence of the magnetic field on the melting and solidification behavior of narrow-gap laser welding with filler wire. The International Journal of Advanced Manufacturing Technology, 2022. **123**(3): p. 1123-1131.

[15] Brata Mohanty, A.S.S., Effects of External Magnetic Field on Mechanical properties of a welded MS metal through Metal Shield Arc Welding.

[16] Hu, C., et al., EBSD study on magnetic field altering crystal texture and grain growth during laser-hybrid welding. Materials & Design, 2022. **216**: p. 110587.

[17] Nguyen, T., et al., The humping phenomenon during high speed gas metal arc welding. Science and Technology of Welding and Joining, 2005. **10**(4): p. 447-459.

[18] Nguyen, T., et al., High speed fusion weld bead defects. Science and Technology of Welding and Joining, 2006. **11**(6): p. 618-633.

[19] Abebe, D.G. and T.M. Bogale, Optimization of TIG welding process parameters on 304 austenitic stainless steel sheet metal using fuzzy logic based Taguchi method. Engineering Research Express, 2023. **5**(4): p. 045045.

[20] N.HarshaVardhana Prakash, B.L.S., K.Srinivasa Rao, Optimization of Welding Parameters to Enhance Mechanical Properties of Az31b Magnesium Alloy Gta Welds. Journal of Harbin Engineering University, 2024. **45**(4): p. 176-185.